CrossMark

ORIGINAL PAPER

Effect of microstructure on chemical stability and electrical properties of $BaCe_{0.9}Y_{0.1}O_{3-\delta}$

Agnieszka Lacz[1]

**Abstract** Y-doped barium cerate $BaCe_{0.9}Y_{0.1}O_{3-\delta}$ was synthesised by a solid-state reaction method. Materials with different average grain sizes and grain boundary surface areas were obtained. The effect of microstructure on the chemical stability in the CO_2 and H_2O-containing atmosphere and electrical properties was analysed and discussed. To evaluate the chemical stability of $BaCe_{0.9}Y_{0.1}O_{3-\delta}$, the exposure test was performed. Samples were exposed to the carbon dioxide and water vapour-rich atmosphere at 25 °C for 700 h. Thermogravimetry supplied by mass spectrometry was applied to analyse the samples before and after this comprehensive test. The mass loss for samples before and after the test and the amount of $BaCO_3$ formed during the test were directly treated as the measure of chemical instability of $BaCe_{0.9}Y_{0.1}O_{3-\delta}$ in the atmosphere rich in carbon dioxide and water vapour. As it was observed, the $BaCe_{0.9}Y_{0.1}O_{3-\delta}$ chemical stability towards CO_2 and H_2O is not affected by the materials' microstructure. Electrical properties of $BaCe_{0.9}Y_{0.1}O_{3-\delta}$ which differs with microstructure were determined using electrochemical impedance spectroscopy (EIS). It was found that the grain interior resistivity and activation energy of grain interior conductivity is microstructure independent. However, the effect on microstructure was seen on the EIS spectra in the range of grain boundary contribution. Therefore, the lowest activation energy and the highest conductivity were observed for a material with the lowest grain boundary surface area.

✉ Agnieszka Lacz
  alacz@agh.edu.pl

[1] Faculty of Materials Science and Ceramics, AGH University of
  Science and Technology, al. Mickiewicza 30,
  30-059 Kraków, Poland

Introduction

Materials based on barium cerate are widely study as potential proton-conducting solid-state electrolytes. One of the most investigated systems is $BaCeO_3$ doped with trivalent ions Me^{3+}, e.g. Y^{3+} or Yb^{3+} [1–4], according to the following equation (Kröger-Vink notation used):

$$2Ce_{Ce}^{x} + O_O^x + Me_2O_3 \rightarrow 2Me_{Ce}^{'} + V_O^{\bullet\bullet} + 2CeO_2 \qquad (1)$$
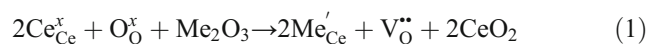
Creation of oxygen vacancies plays an important role in proton conduction which appears in water vapour and hydrogen-containing atmosphere. However, insufficient chemical stability in the CO_2 and H_2O-rich atmospheres is still one of the greatest disadvantages of this type of materials, results in a decrease of mechanical properties and leads to disintegration of materials.

For polycrystalline materials, the contribution of grain boundaries is inversely proportional to the grain size, as the reduction of grain size simply leads to an increase of the contact area. Consequently, the amount of grain boundaries increases. Concerning the blocking effect of grain boundaries especially for barium zirconate and barium cerate materials, the increase of total conductivity can be observed for small-grain size samples. The effect of microstructure on electrical properties of $BaCeO_3$-based materials was not extensively studied. Generally, the electrical properties of grain interior are not affected by the microstructure. The conductivity and the activation energy of grain interior conductivity are irrespective to the size of the grains [5, 6]. However, an influence of a synthesised procedure can be observed [7]. The effect of

🖄 Springer

microstructure on the grain boundary electrical properties seems to be a more complex issue. As it was reported for gadolinium and niobium-doped barium cerate, the specific grain boundary conductivity seems to be independent on the grain size [8, 9]. Though, the activation energy of grain boundary conductivity shows significant changes with the microstructure [10]. For materials based on barium compounds sintered in the relatively high temperature, the change in the composition of grain boundaries caused by e.g. barium vaporisation or segregation of second phases on the grain boundaries can result in a decrease of grain boundary conductivity [5].

The insufficient chemical stability of $BaCeO_3$-based materials is the result of the tendency of barium cerate to convert to barium carbonate or barium hydroxide in CO_2 and H_2O-containing atmospheres according to the following reactions:

$$BaCeO_3 + CO_2 \rightarrow BaCO_3 + CeO_2 \qquad (2)$$

$$BaCeO_3 + H_2O \rightarrow Ba(OH)_2 + CeO_2 \qquad (3)$$
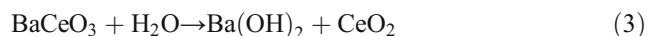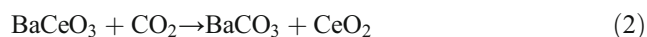
The thermodynamic data suggest that barium cerate is an unstable phase in the wide temperature range [11–13]. The ΔG of the reaction of barium carbonate formation (Eq. 2) is negative at 25 °C; however, it increases with temperature. It implies that stability of $BaCeO_3$ towards carbon dioxide rises with temperature. Chemical stability of $BaCeO_3$-based materials in CO_2 and water vapour is widely discussed in the literature; however, the working conditions (temperature 400–750 °C) of devices made of barium cerate [14–17] are mainly considered. Nevertheless, the effect of microstructure on chemical stability of this type of materials was not yet analysed. It should be mentioned that the chemical stability of $BaCeO_3$-based materials analysed in this work refers to room temperature (25 °C) and simulates the storage conditions of electrochemical devices made of barium cerate-based materials.

The purpose of this work is to determine the influence of microstructure on the chemical stability and electrical properties of 10 % mol Y-doped barium cerate. This comprehensive study regards to the stability of $BaCe_{0.9}Y_{0.1}O_{3-\delta}$ towards CO_2 and water vapour at low-temperature exposure (simulating storage conditions) along with the analysis of $BaCe_{0.9}Y_{0.1}O_{3-\delta}$ grain interior and grain boundary electrical properties.

Experimental

Samples of Y-doped barium cerate were synthesised by a solid-state reaction method. All reagents used during material synthesis were delivered by Aldrich Chemical Company Inc.: barium carbonate ($BaCO_3$, ≥99 %), cerium(IV) oxide (CeO_2, 99.9 %) and yttrium oxide (Y_2O_3, 99.99 %). Powders were

mixed and impregnated with the yttrium oxide solution in nitric acid (concentration 0.36 M), dried at 85 °C for 12 h and crushed in the agate mortar. The prepared mixture of the precursor was formed in the pellet die and calcinated at 1200 °C for 24 h. Obtained materials were crushed, milled in absolute alcohol suspension (ZrO_2 grinding media) and, after drying, formed in a pellet die, isostatically pressed (2.0 MPa) and sintered in air at 1600 °C. The only difference between the samples was the time of sintering; 3, 6, 9 and 24 h of sintering were applied. All prepared materials were stored in the desiccator to avoid any secondary reactions.

To define the phase composition and crystallographic structure of sintered materials, the X-ray diffraction (Philips X'Pert with CuKα radiation) was applied. Microstructure characterisation was performed based on scanning electron microscopy (SEM) (Nova NanoSEM 200 FEI and Oxford Instruments).

To evaluate the chemical stability of the samples for CO_2 and H_2O, the comprehensive exposure test was performed. Samples were exposed to the carbon dioxide and water vapour-containing atmosphere (7 % CO_2 in air, 100 % relative humidity (RH)) at 25 °C for 700 h. All samples before and after the exposure test were heated in the SDT 2960 TA Instruments apparatus (mass of samples 50 mg, heating rate 10 °C/min, synthetic air flow) coupled with the QMD 300 ThermoStar Balzers mass spectrometer.

The electrical properties were determined based on electrochemical impedance spectroscopy (EIS) measurements carried out in the frequency response analyser FRA 1260 coupled with the dielectric interface (DI) 1296A (both from Solartron Analytical Inc., USA). The measurements were performed on sintered pellets as a function of temperature (20–500 °C) for three gas atmospheres: synthetic air, water vapour-saturated synthetic air and 5 % H_2 in Ar. The measurements were performed in the frequency range of 10^{-1}–10^6 Hz with the amplitude of sinusoidal voltage of 0.02 V. Before each measurement, samples were equilibrated for at least 30 min at given conditions (temperature and gas atmosphere). The values of equivalent circuit components were determined using ZView 2.0 software (Scribner Asc., USA).

Results and discussion

Structure and microstructure

Concerning the relatively high sintering temperature and the extended time of sintering, the barium vaporisation from the samples was observed. Sintered samples were polished for removing the surface barium-deficient layer to minimise the Ba-deficit effect and to standardise the chemical composition of all samples tested. All measurements were performed on polished materials. Figure 1 shows the comparison of X-ray
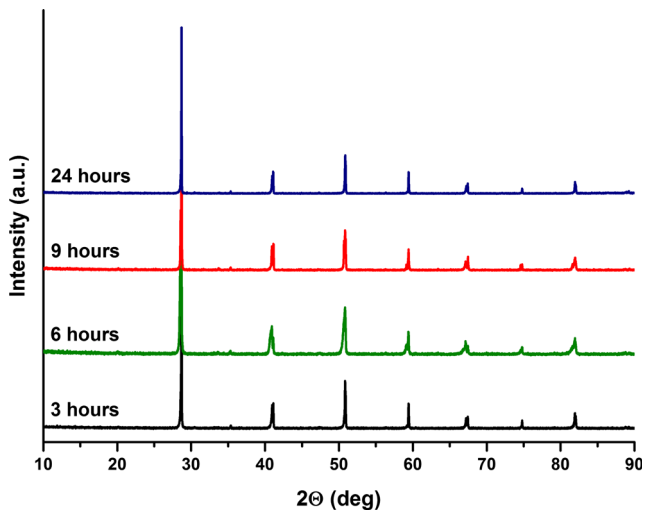
Fig. 1 XRD results of $BaCe_{0.9}Y_{0.1}O_{3-\delta}$ with different sintering times

diffraction (XRD) data for samples sintered for different times. It was found that for all $BaCe_{0.9}Y_{0.1}O_{3-\delta}$ samples, a single-phase perovskite material was formed, interpreted as orthorhombic (space group Pmcn, ICSD collection code: 79001). However, slight differences in texture were observed.

The effect of sintering time on microstructure is shown in Fig. 2. SEM microphotographs were performed on fractured samples. The extension of sintering time leads to an increase of the average grain size from 2.5–4.0 μm for 3 h of sintering to 8.0–12.0 μm for 24 h of sintering. Moreover, for relatively long sintering time (9–24 h), the results of material defects, e.g. dislocations, can be observed. The stereology was applied to estimate the close porosity and grain boundary surface area [18]. The results are summarised in Table 1. Extensions of sintering time leads to significant changes in the $BaCe_{0.9}Y_{0.1}O_{3-\delta}$ microstructure. The porosity is comparable for all samples, but the amount of grain boundaries, which is strongly correlated with the grain size, is sintering time dependent. After 3 h of $BaCe_{0.9}Y_{0.1}O_{3-\delta}$ sintering, the average grain size is 2.5–4.0 μm and the grain boundary surface area is about 0.70 $\mu m^2/\mu m^3$. A twofold increase of sintering time
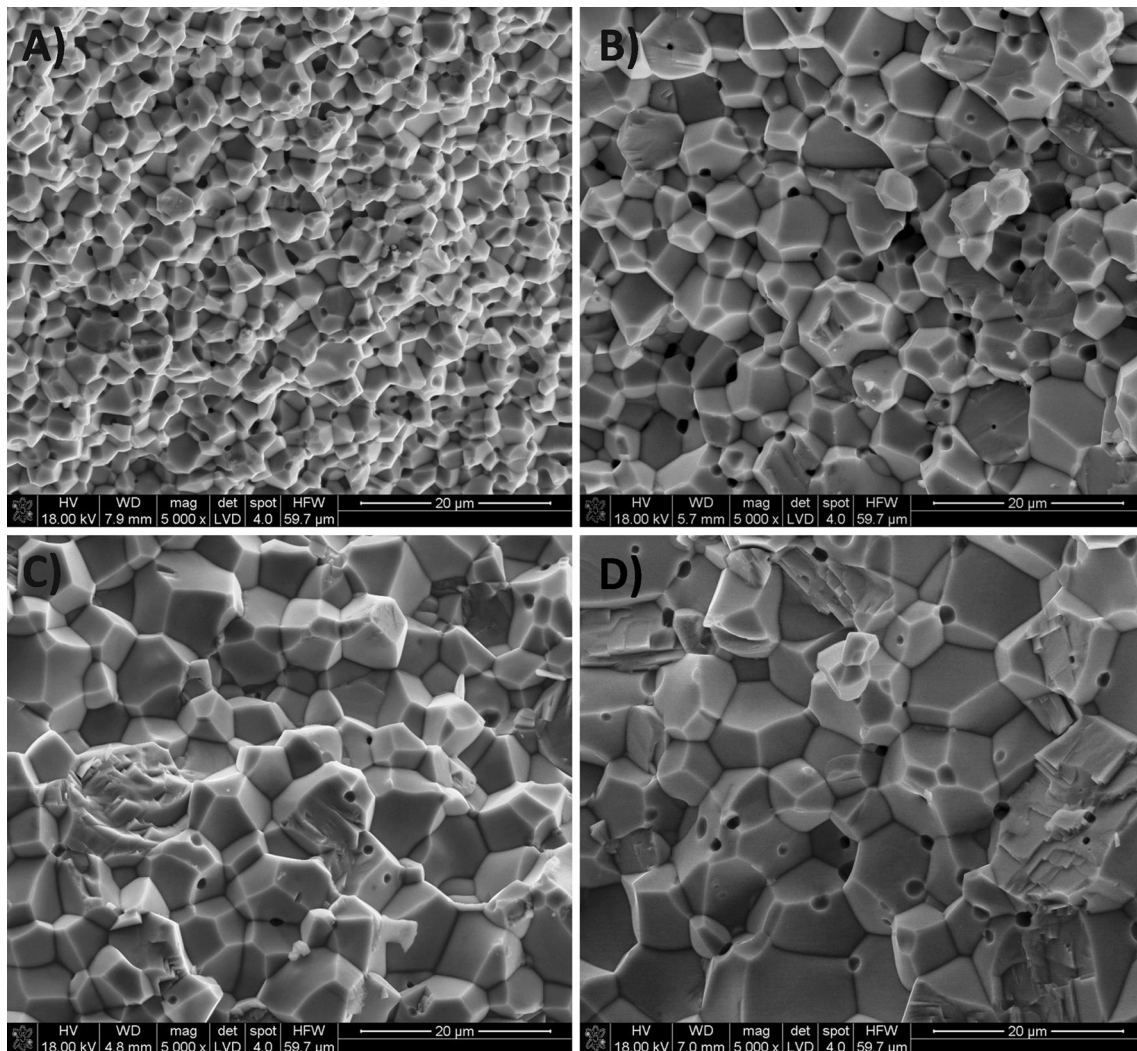

Fig. 2 SEM microphotographs of surface fracture of $BaCe_{0.9}Y_{0.1}O_{3-\delta}$-sintered samples. Time of sintering: 3 (**a**), 6 (**b**), 9 (**c**) and 24 (**d**) h

**Table 1** Grain size, porosity and grain boundary surface area of $BaCe_{0.9}Y_{0.1}O_{3-\delta}$ materials

	Sintering time			
	3 h	6 h	9 h	24 h
Average grain size (μm)	2.5–4.0	5.0–7.0	6.0–9.0	8.0–12.0
Porosity (%)	2.5 ± 0.3	3.0 ± 0.5	1.5 ± 0.5	2.5 ± 0.6
Grain boundary surface area (μm²/μm³)	0.70 ± 0.05	0.35 ± 0.02	0.30 ± 0.03	0.25 ± 0.01

(up to 6 h) results in almost double enlargement of $BaCe_{0.9}Y_{0.1}O_{3-\delta}$ grain size (5.0–7.0 μm) and double reduction of the surface area of grain boundary (0.35 μm²/μm³). Extension of sintering time to 9 and 24 h leads to a progressive increase of grain size (6.0–9.0 and 8.0–12.0 μm, respectively) and a decrease of grain boundary surface area (0.30 and 0.25 μm²/μm³, respectively), but these changes are not tremendous.

In summary, the time of sintering strongly affects the microstructure of $BaCe_{0.9}Y_{0.1}O_{3-\delta}$ materials, mainly the grain size and grain boundaries properties. The crystallographic structure is sintering time independent; however, the long sintering time can result in a difference of the samples' texture.

Chemical stability

The poor chemical stability in the corrosive atmosphere is one of the greatest disadvantages of the materials based on barium cerate. Thermal analysis combined with mass spectrometry was already established as the proper tool for evaluation of the chemical stability of $BaCeO_3$-based materials [19, 20]. All samples were exposed to the CO_2 and H_2O-containing atmosphere for the same period of time which allows the comparative analysis. During this exposure test, barium carbonate and barium hydroxide formation can proceed as the result of $BaCeO_3$ reaction with CO_2 and H_2O, respectively (Eqs. 2 and 3). The XRD analysis of the sample after the exposure test (Fig. 3) shows the presence of barium carbonate: the result of the reaction runs during the test. The second phase is
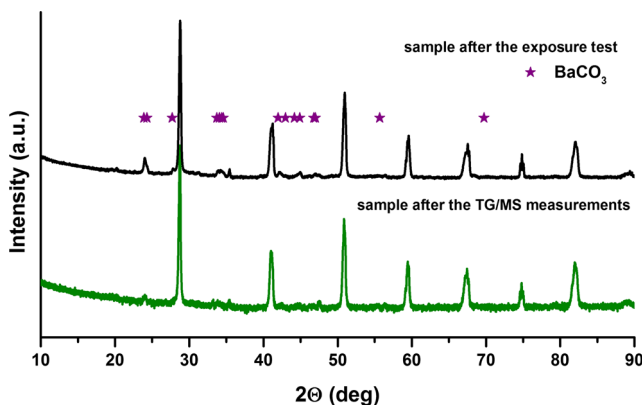
Fig. 3 XRD results of $BaCe_{0.9}Y_{0.1}O_{3-\delta}$ sample after the exposure test (*black line*) and after the TG/MS measurements (*green line*)

orthorhombic (Pmcn) barium cerate. However, for the low values of 2θ, the increase of background suggests the presence of amorphous phase, probably the barium hydroxide and/or cerium(IV) oxide, the second product of conversation reaction of barium cerate to barium carbonate. Figure 4 shows the thermogravimetry (TG) curves for samples before and after the exposure test. The mass loss observed for all samples before the test does not exceed 0.3 % and is connected with the degradation of materials in the temperature range 500–700 °C. For materials after the exposure test, the shape of TG curve is also similar for all samples tested. Moreover, three regions on TG curves can be distinguished with the total mass loss around 1.2–1.5 %. The first region covers the temperature range 30–300 °C, the second one 300–775 °C and the last one temperatures above 775 °C.

The TG curves supplied by mass spectrometry (MS) results are presented in Fig. 5. Ion current lines for $m/z = 18$ and $m/z = 44$ describe evolving water and carbon dioxide during the thermal treatment of the samples. The first region on TG curve (below 300 °C) can be treated as dehydration of the samples and removing the water absorbed on the samples' surface or in the pores during the test. However, for samples before the test, this process is irrelevant due to the lack of mass loss below 300 °C. The samples' behaviour described in the second region on TG curves differs from that of the materials before and after the test. For samples before the test, thermogravimetry curve and $m/z = 18$ ion current line imply liberation of water from all samples regardless the sintering time applied. The mass loss calculated for the temperature range 450–750 °C for all samples is about 0.30 %. The relatively high temperature (above 500 °C) excludes releasing of the absorbed water. The XRD analysis of initial samples showed single-phase barium cerate. Thus, the H_2O evolved in high temperature should be the result of processes run in the samples. Probably, it can be the effect of destruction of the protonic defects in $BaCe_{0.9}Y_{0.1}O_{3-\delta}$ as shown in the following reaction:

$$2OH_O^{\bullet} \leftrightarrow H_2O + O_O^x + V_O^{\bullet\bullet} \tag{4}$$

Especially, that amount of yttrium which, indirectly, is the protonic defect cause is the same for all samples and the mass loss for all samples before the test is very similar. Moreover, for samples after the test, a similar behaviour is observed, namely liberation of water in the temperature range 500–

Fig. 4 TG curves of BaCe$_{0.9}$Y$_{0.1}$O$_{3-\delta}$ decomposition before and after the exposure test
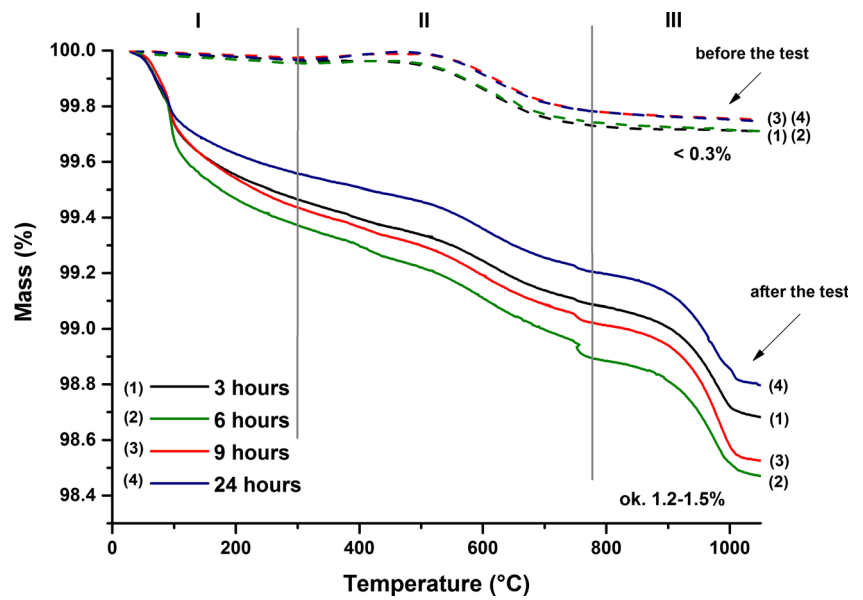
700 °C. Unfortunately, the lack of *plateau* on TG curves excludes the precise calculation of mass loss. However, the comparison of $m/z = 18$ ion current line for samples before and

after the test for different sintering times (Fig. 6) implies that analysed effect is sintering conditions and exposure experiment independent.
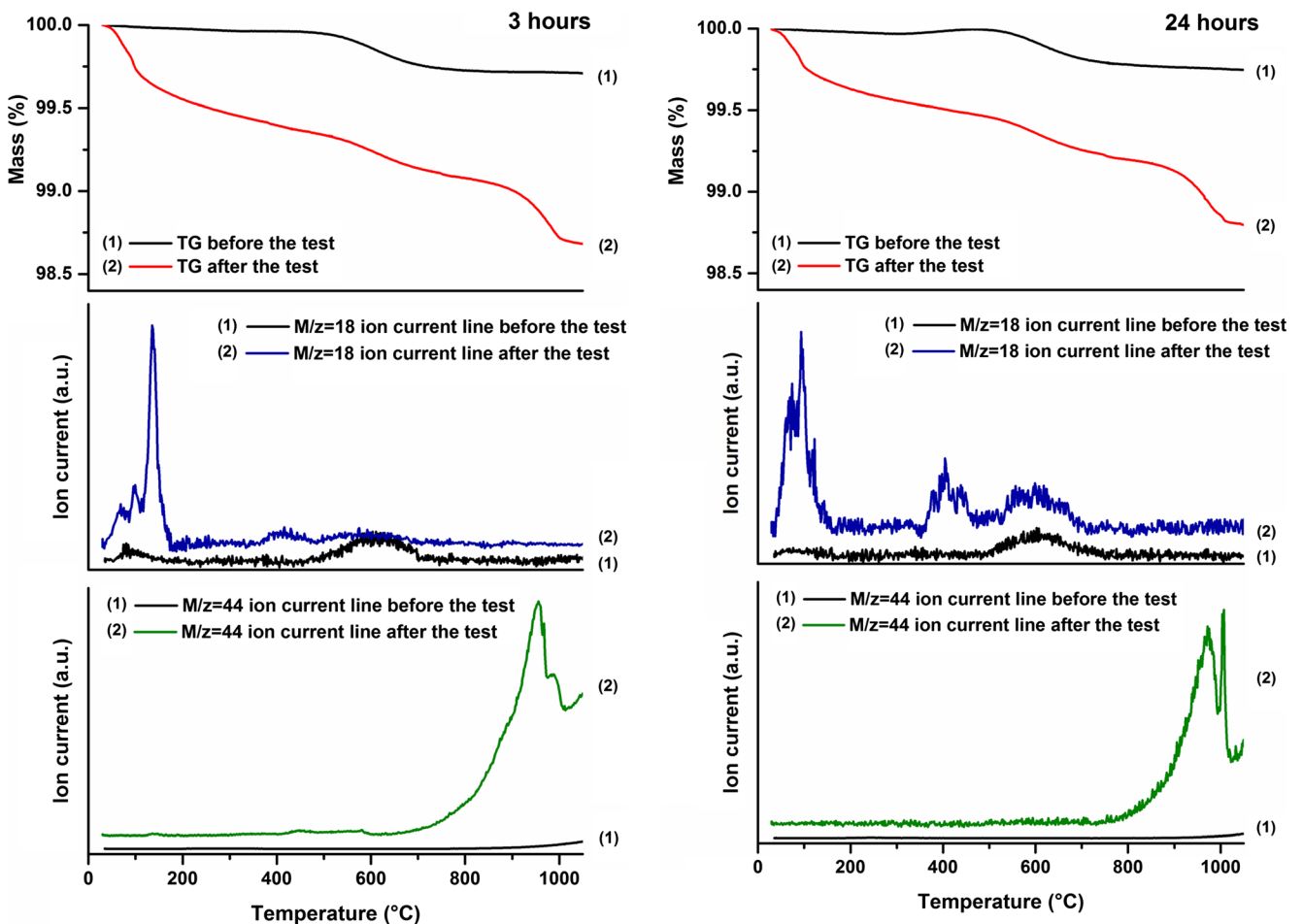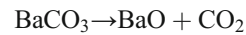

Fig. 5 TG curves and $m/z = 18$ and $m/z = 44$ ion current lines of BaCe$_{0.9}$Y$_{0.1}$O$_{3-\delta}$ decomposition before and after the exposure test (3 and 24 h of sintering)

Figures 5 and 6 clearly show that for samples after the test, an additional effect combined with releasing water is observed in the range 350–500 °C. It can be attributed to the decomposition of barium hydroxide $Ba(OH)_2$ formed during the exposure test as the result of $BaCeO_3$ reaction with H_2O (Eq. 3) which was also reported in [21]. According to the literature, the decomposition temperature of pure $Ba(OH)_2$ is about 410 °C [22]. It should be noticed that the amount of barium hydroxide in the samples after the test is impossible to calculate or even to estimate based on TG curve. The $Ba(OH)_2$ decomposition step is not clearly separated and overlaps with the step of protonic defect degradation. The slight mass loss suggests that the amount of formed $Ba(OH)_2$ is significantly low. Moreover, the XRD analysis of the samples after the test does not show the presence of crystalline barium hydroxide. Probably, the amount of $Ba(OH)_2$ was below the detection point of the method applied or barium hydroxide was amorphous.

The last stage of sample degradation (region III, Fig. 4) is seen only for samples after the test, and it is connected with releasing CO_2 (Fig. 5) as the only gaseous product. The XRD analysis of the samples after the test (Fig. 3)

clearly shows the presence of barium carbonate; the result of the reaction between barium cerate and CO_2 runs during the exposure test. Three mechanisms of the last stage of degradation were considered:
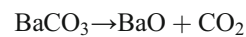
1. Decomposition of barium carbonate

$$BaCO_3 \rightarrow BaO + CO_2$$

2. Reverse reaction to the reaction proceed during the test

$$BaCO_3 + CeO_2 \rightarrow BaCeO_3 + CO_2$$
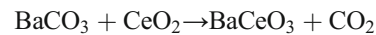
3. Two-step reaction of $BaCeO_3$ formations

$$BaCO_3 \rightarrow BaO + CO_2$$

$$BaO + CeO_2 \rightarrow BaCeO_3$$

All proposed ways of material degradation in the last stage lead to the same mass loss and the same gaseous product (CO_2). According to the XRD results for samples after the TG/MS measurement (Fig. 3), the major crystalline phase is orthorhombic (Pmcn) barium cerate. However, the presence of amorphous phase with an
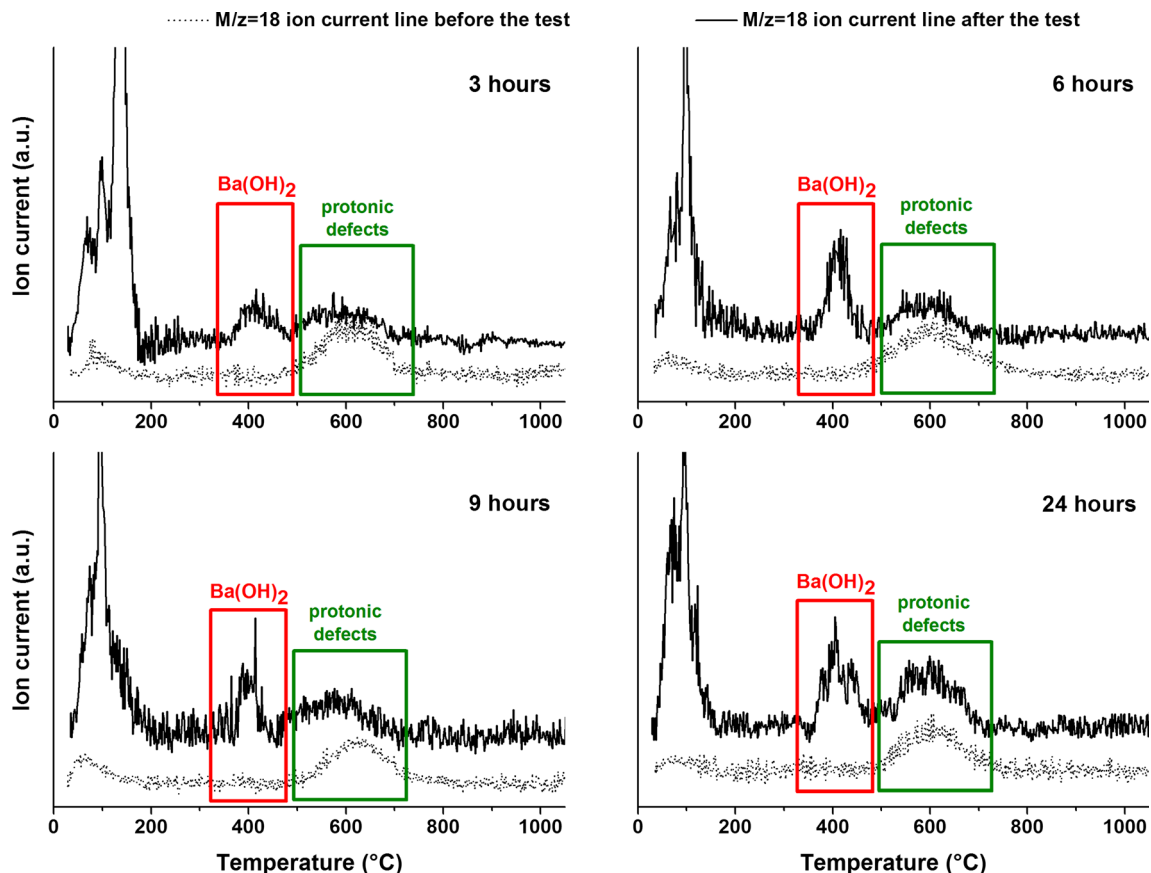

Fig. 6 $m/z = 18$ ion current lines of $BaCe_{0.9}Y_{0.1}O_{3-\delta}$ decomposition before and after the exposure test for different sintering times

Table 2 BaCO$_3$ content in the initial BaCe$_{0.9}$Y$_{0.1}$O$_{3-\delta}$ samples after the exposure test

	Sintering time			
	3 h	6 h	9 h	24 h
% of BaCO$_3$	1.8	1.9	2.2	1.8

unidentified composition is also seen. Concerning the TG/MS procedure, especially the short time of sample exposure to the relatively high temperature (1000–1100 °C), the first possibility, decomposition of barium carbonate, formed during the exposure test, seems to be the most probable reaction occurred. However, it can only be supposed, not definitely stated. The calculations performed based on TG curve allow to evaluate BaCO$_3$ content in the BaCe$_{0.9}$Y$_{0.1}$O$_{3-\delta}$ samples after the exposure test (Table 2). As it was observed, the amount of formed barium carbonate was comparable for samples with different microstructures. Thus, it can be suggested that the chemical stability of BaCe$_{0.9}$Y$_{0.1}$O$_{3-\delta}$ towards CO$_2$ is not affected by the materials' microstructure. The differences in the TG shape and the total mass loss are mainly the results of different mass losses in the first step of decomposition, namely the ability to absorb water.

Electrical properties

In order to determine the influence of the BaCe$_{0.9}$Y$_{0.1}$O$_{3-\delta}$ microstructure on the electrical properties, the electrochemical impedance spectroscopy (EIS) measurements were performed as a function of temperature (20–500 °C) and gas atmosphere (synthetic air, water vapour-saturated synthetic air and 5 % H$_2$ in Ar). The introduction of Y into cerium position in BaCeO$_3$ leads to the creation of the oxygen ion vacancies which result in oxygen ion conductivity in inert and dry atmospheres. However, in higher temperatures, hole conductivity may also be observed [23]. In water or hydrogen-containing atmospheres, the proton conductivity appears. Concerning the temperature of EIS measurements (up to 500 °C), the results of the oxygen ion conductivity in air and the proton conductivity in 100 % RH air and 5 % H$_2$ in Ar should be observed. Figure 7 shows the representative Nyquist plots obtained for H$_2$ (5 %) in Ar at 423 K for BaCe$_{0.9}$Y$_{0.1}$O$_{3-\delta}$ samples sintered for 3, 6, 9 and 24 h. Two semicircles, corresponding to the grain interior (bulk) and grain boundary impedance, can be observed for all samples. At low frequencies, the part of the spectra related to the electrode can also be noticed. The electrode properties are not discussed in this work; thus, these parts of the spectra were not analysed. The EIS spectra were fitted using the
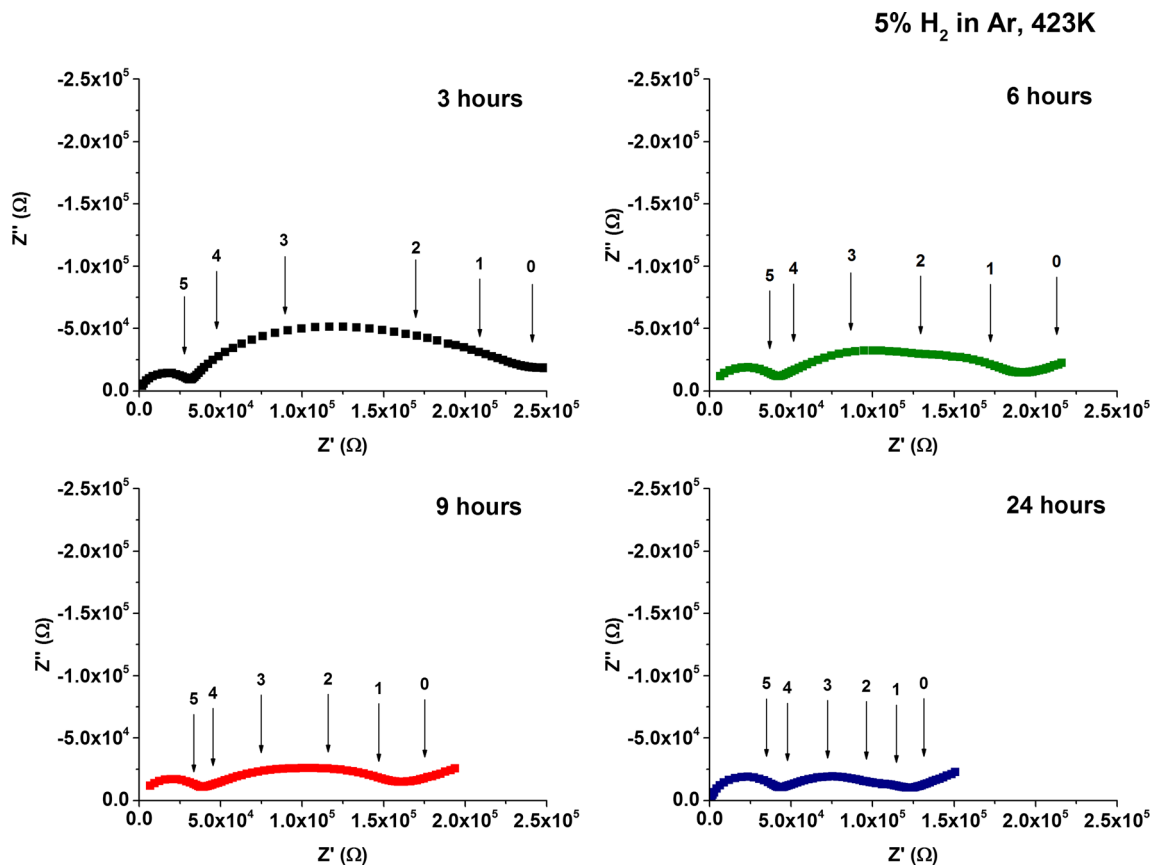

Fig. 7 Nyquist plots of the BaCe$_{0.9}$Y$_{0.1}$O$_{3-\delta}$ with different microstructures in the H$_2$ atmosphere (5 % in Ar) at 423 K

equivalent circuit consisting of two connections in series sets of resistors (Rs) and constant phase elements (CPEs) connected in parallel related to bulk and grain boundary contribution, respectively. Assignment of R1 and R2 values to the resistance of grain interior and grain boundary was performed based mainly on the CPE values. The obtained capacitance values were found to be in the range of 10^{-11}–10^{-10} and 10^{-9}–10^{-8} F for CPE1 and CPE2, respectively, independent of the gas atmosphere. These values are typical for bulk and grain boundary properties [24]. Consequently, R1 and CPE1 elements can be interpreted as resistance and capacitance of bulk. Furthermore, R2 and CPE2 elements can be assigned to grain boundary resistance and grain boundary capacitance, respectively. The grain interior conductivity (σ_{gi}) and the grain boundary conductivity (σ_{gb}) were calculated concerning the geometry of the sample and grain interior resistance (R_{gi}) or grain boundary resistance (R_{gb}) obtained based on the EIS measurements: $\sigma_{gi/gb} = L/(A \cdot R_{gi/gb})$, where L and A are the

sample thickness and the electrode area, respectively. Figure 8 presents the obtained results in Arrhenius coordinates. The resistivity of bulk depends on the temperature and gas atmosphere (Fig. 8). However, for the same temperature and gas atmosphere, the grain interior resistivity value is comparable for samples sintered for 3, 6, 9 and 24 h (Figs. 7 and 8). Therefore, it can be suggested that bulk resistivity does not depend on the microstructure of the material. Moreover, the activation energy (E_a) of grain interior conductivity, calculated based on Arrhenius plots and summarised in Table 3, is atmosphere and microstructure independent. The determined value of E_a about 0.50 eV is in agreement with previously reported values for $BaCe_{0.9}Y_{0.1}O_{3-\delta}$ materials [6, 25].

The resistivity of grain boundary depends on the temperature and gas atmosphere, which is similar as it was observed for bulk contribution. However, the effect of microstructure is also seen. The changes in the resistivity are not significant;
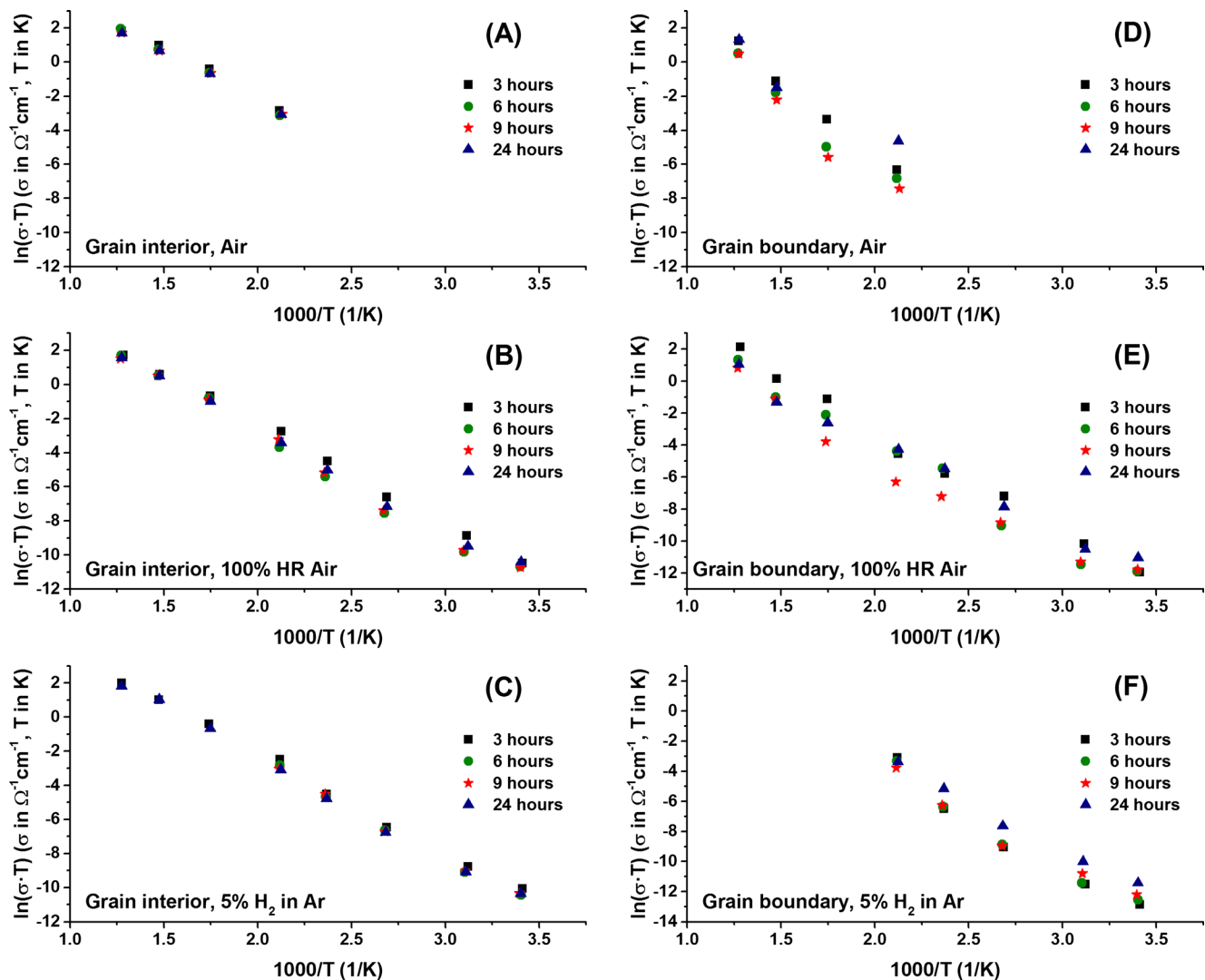

Fig. 8 Arrhenius plots for $BaCe_{0.9}Y_{0.1}O_{3-\delta}$ samples with different microstructures under dry air, wet air (100 % RH) and H_2 (5 % in Ar) atmospheres

Table 3 Activation energies E_a determined from EIS measurements

Sintering time (h)	Activation energy (E_a, eV)					
	Air		100 % RH air		5 % H_2 in Ar	
	Bulk	Grain boundary	Bulk	Grain boundary	Bulk	Grain boundary
3	0.48 ± 0.03	0.76 ± 0.05	0.50 ± 0.01	0.56 ± 0.02	0.50 ± 0.01	0.63 ± 0.07
6	0.51 ± 0.02	0.75 ± 0.11	0.53 ± 0.02	0.55 ± 0.03	0.51 ± 0.02	0.61 ± 0.07
9	0.48 ± 0.02	0.80 ± 0.13	0.52 ± 0.02	0.51 ± 0.04	0.50 ± 0.02	0.55 ± 0.06
24	0.48 ± 0.02	0.56 ± 0.15	0.51 ± 0.01	0.48 ± 0.02	0.51 ± 0.01	0.54 ± 0.03

nevertheless, concerning the sintering time, some observation can be made. For the same temperature and atmosphere, the differences in resistivity for samples sintered for 3, 6, 9 and 24 h usually do not exceed half of order or an order of magnitude. The resistivity of the sample sintered for 24 h is generally the lowest for most of the cases. Moreover, the activation energy of grain boundary conductivity depends on the atmosphere and microstructure (Table 3). The values of activation energy of grain boundary conductivity clearly suggest the different mechanisms of conductivity in wet air/hydrogen in Ar (proton conductivity) and dry synthetic air (oxygen ion conductivity). The calculated values stay in agreement with the literature data. The activation energy of proton conductivity is reported to be 0.5–0.6 eV [26, 27], and for oxide ion conductivity, the activation energy is about 0.75–0.8 eV [23]. The effect of materials' microstructure is reflected in the values of E_a. The activation energy of grain boundary conductivity decreases with increasing the sintering time. Accordingly, for the highest grain boundary surface area (sample after 3 h of sintering), the E_a reaches the highest value for all atmospheres. Figure 9 shows the dependence of activation
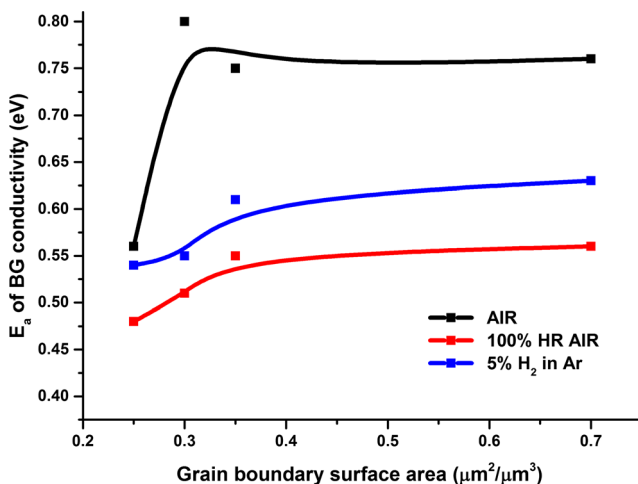
energy on the materials' microstructure understood as the volume of grain boundary surface area. This comparison suggests that two factors affect the E_a of grain boundary conductivity. The average grain size is one of them. However, it should be noticed that extension of sintering time to 24 h leads not only to the decrease of grain boundary volume but also to the imperfection of grain boundaries (Fig. 2). Thus, the influence of grain boundary defects on the activation energy of grain boundary conductivity cannot be excluded.

Conclusions

The solid-state reaction method was applied to synthesise the $BaCe_{0.9}Y_{0.1}O_{3-\delta}$ which differs with the microstructure. The comparative exposure test (7 % CO_2 in air, 100 % RH, 25 °C, 700 h) allowed to evaluate the chemical stability of Y-doped barium cerate towards CO_2 and H_2O. The amount of formed barium carbonate was comparable for samples with different microstructures the same as the total mass loss. Thus, the $BaCe_{0.9}Y_{0.1}O_{3-\delta}$ chemical stability towards CO_2 and H_2O is not affected by the materials' microstructure. It can be suggested that the grain boundaries are not involved in barium cerate conversion to barium carbonate or barium hydroxide and are not responsible for the chemical instability of $BaCe_{0.9}Y_{0.1}O_{3-\delta}$ in the corrosive gas atmosphere.

Based on EIS measurements, the grain interior and grain boundary contribution to the conductivity of $BaCe_{0.9}Y_{0.1}O_{3-\delta}$ was estimated. It was observed that grain interior conductivity and its activation energy are microstructure independent. The slightly effect of grain size was noticed for the conductivity of grain boundary. Moreover, the differences in the activation energy of grain boundary conductivity were not significant but the trend was clearly seen, namely the decrease of E_a with a decrease of the grain boundary surface area. Thus, the microstructure can slightly influence only the grain boundary electrical properties of $BaCe_{0.9}Y_{0.1}O_{3-\delta}$.

Fig. 9 f Activation energy of grain boundary conductivity as a function of grain boundary surface area for dry air, wet air (100 % RH) and H_2 (5 % in Ar) atmospheres

References

1. Chiodelli G, Malavasi L, Tealdi C, Barison S, Battagliarin M, Doubova L, Fabrizio M, Mortalo C, Gerbasi R (2009) Role of synthetic route on the transport properties of $BaCe_{1-x}Y_xO_3$ proton conductor. J Alloys Compd 470:477–485. doi:10.1016/j.jallcom.2008.03.011

2. Osman N, Talib IA, Hamid HA, Jani AM (2008) Characterization, electrical conduction and stability of Yb-doped barium cerate prepared by sol-gel method. Ionics 14:407–413. doi:10.1007/s11581-007-0184-x

3. Medvedev D, Murashkina A, Pikalova E, Demin A, Podias A, Tsiakaras P (2014) $BaCeO_3$: materials development, properties and application. Prog Mater Sci 60:72–129. doi:10.1016/j.pmatsci.2013.08.001

4. Vaquero-Aguilar C, Jimenez-Melendo M (2011) Characterization and creep properties of proton-conducting Yb-doped barium cerate. J Eur Ceram Soc 31:2671–2676. doi:10.1016/j.jeurceramsoc.2011.01.001

5. Wang S, Zhao F, Zhang L, Chen F (2012) Synthesis of $BaCe_{0.7}Zr_{0.1}Y_{0.1}Yb_{0.1}O_{3-\delta}$ proton conducting ceramic by a modified Pechini method. Solid State Ion 213:29–35. doi:10.1016/j.ssi.2011.05.014

6. Bassano A, Buscagli V, Viviani M, Bassoli M, Buscagli MT, Sennour M, Thorel A, Nanni P (2009) Synthesis of Y-doped $BaCeO_3$ nanopowders by a modified solid-state process and conductivity of dense fine-grained ceramics. Solid State Ion 180:168–174. doi:10.1016/j.ssi.2008.12.026

7. Sawant P, Varma S, Wani BN, Bharadwaj SR (2012) Influence of synthesis route on morphology and conduction behavior of $BaCe_{0.8}Y_{0.2}O_{3-\delta}$. J Therm Anal Calorim 107:189–195. doi:10.1007/s10973-011-1658-7

8. Rauch WL, Liu ML (1997) Effect of microstructure and dopant on the electrochemical properties of barium cerate-based electrolytes. Proceedings of The First International Symposium on Ceramic Membranes Electrochemical Society Series 95:146–165

9. Haile SM, West DL, Campbell J (1998) The role of microstructure and processing on the proton conducting properties of gadolinium-doped barium cerate. J Mater Res 13:1576–1595. doi:10.1557/JMR.1998.0219

10. Khandelwal M, Venkatasubramanian A, Prasanna TRS, Gopalan P (2011) Correlation between microstructure and electrical conductivity in composite electrolytes containing Gd-doped ceria and Gd-doped barium cerate. J Eur Ceram Soc 31:559–568. doi:10.1016/j.jeurceramsoc.2010.10.027

11. Talimi M, Thangadurai V (2011) Electrical conductivity and chemical stability of perovskite-type $BaCe_{0.8-x}Ti_xY_{0.2}O_{3-\delta}$. Ionics 17:195–200. doi:10.1007/s11581-011-0522-x

12. Cordfunke EHP, Booij AS, Huntelaar ME (1998) The thermochemical properties of $BaCeO_3$ and $SrCeO_3$ from T = 5 to 1500K. J Chem Thermodyn 30:437–447. doi:10.1006/jcht.1997.0302

13. Gopalan S, Virkar AV (1993) Thermodynamic stabilities of $SrCeO_3$ and $BaCeO_3$ using a molten salt method and galvanic cells. J Electrochem Soc 140:1060–1065. doi:10.1149/1.2056197

14. Kim JH, Kang YM, Byun MS, Hwang KT (2011) Study on the chemical stability of Y-doped $BaCeO_{3-\delta}$ and $BaZrO_{3-\delta}$ films deposited by aerosol deposition. Thin Solid Films 520:1015–21. doi:10.1016/j.tsf.2011.08.013

15. Okiba T, Fujishiro F, Hashimoto T (2013) Evaluation of kinetic stability against CO_2 and conducting property of $BaCe_{0.9-x}Zr_xY_{0.1}O_{3-\delta}$. J Therm Anal Calorim 113:1269–74. doi:10.1007/s10973-013-3205-1

16. Azad AK, Irvine JTS (2007) Synthesis, chemical stability and proton conductivity of the perovksites Ba(Ce, Zr)1-xScxO3-δ. Solid State Ion 178:635–40. doi:10.1016/j.ssi.2007.02.004

17. Ryu KH, Haile SM (1999) Chemical stability and proton conductivity of doped $BaCeO_3$-$BaZrO_3$ solid solutions. Solid State Ion 125:355–67. doi:10.1016/S0167-2738(99)00196-4

18. Russ JC, Dehoff RT (2000) Practical stereology, 2nd edn. Springer

19. Haile SM, Staneff G, Ryu KH (2001) Non-stoichiometry, grain boundary transport and chemical stability of proton conducting perovskites. J Mater Sci 36:1149–1160. doi:10.1023/A:1004877708871

20. Pasierb P, Gajerski R, Osiadły M, Łącz A (2014) Application of DTA-TG-MS for determination of chemical stability of $BaCeO_{3-\delta}$-based protonic conductors. J Therm Anal Calorim 117:683–691. doi:10.1007/s10973-014-3746-y

21. Slodczyk A, Sharp MD, Upasen S, Colomban P, Kilner JA (2014) Combined bulk and surface analysis of the $BaCe_{0.5}Zr_{0.3}Y_{0.16}Zn_{0.04}O_{3-\delta}$ (BCZYZ) ceramic proton-conducting electrolyte. Solid State Ion 262:870–874. doi:10.1016/j.ssi.2013.12.044

22. Habashy GM, Kolta GA (1972) Thermal-decomposition of hydrates of barium hydroxide. J Inorg Nucl Chem 34:57–67. doi:10.1016/0022-1902(72)80361-0

23. Jadhav ST, Dubal SU, Jamale AP, Patil SP, Bhosale CH, Puri VR, Jadhav LD (2015) Structural, morphological and electrical studies of $BaCe_{0.8}Y_{0.2}O_{3-\delta}$ synthesized by solution combustion method. Ionics 21:1295–1300. doi:10.1007/s11581-014-1304-z

24. Barsoukov E, Macdonald JR (2005) Impedance spectroscopy theory, experiment, and applications, 2nd edn., Wiley-Interscience.

25. Lacz A, Grzesik K, Pasierb P (2015) Electrical properties of $BaCeO_3$-based composite protonic conductors. J Power Sources 279:80–87. doi:10.1016/j.jpowsour.2014.12.065

26. Ruiz-Trejo E, Irvine JTS (2012) Ceramic proton conducting membranes for the electrochemical production of syngas. Solid State Ion 216:36–40. doi:10.1016/j.ssi.2012.01.033

27. Sherafat Z, Paydar MH, Antunes I, Nasani N, Brandão AD, Fagg DP (2015) Modeling of electrical conductivity in the proton conductor $Ba_{0.85}K_{0.15}ZrO_{3-\delta}$. Electrochim Acta 165:443–449. doi:10.1016/j.electacta.2015.03.018